nature communications

Article

https://doi.org/10.1038/s41467-025-63252-1

Anomalous photoelectrochemical etching of undoped semiconductor surfaces

Received: 25 September 2024

Accepted: 13 August 2025

Published online: 23 August 2025

Check for updates

Pan Peng[1,2,3,8], Xinqin Liu[1,2,3,8], Shuming Yang[4], Renjie Zhou[5], Hui Deng[6], Liang Gao[1], Nicholas X. Fang[7] ✉, Shiyuan Liu[1,3] ✉ & Jinlong Zhu[1,2,3] ✉

For more than 60 years, it has been widely accepted that the irradiance of the incoming light plays the most critical role in the etching effect of the photoelectrochemical etching process, which is built upon the underlying physics that photo-generated charge carriers catalyze the dissolution of n-type semiconductors. However, in this paper, we report an anomalous physical phenomenon, i.e., the spatially distributed photons with a lateral gradient could drive the lateral distribution of carriers on the surface of semiconductors, which leads to the anomalous etching phenomenon on the surface of undoped semiconductor materials during the PEC etching process. Research shows that parameters such as light intensity, light intensity gradient, and carrier diffusion length are significantly correlated with this process. This discovery provides a potential method of rapid and large-scale 3D nanomanufacturing on semiconductor materials, which holds promise for significant applications in diverse fields such as microelectronics, nanophotonics, microelectromechanical systems (MEMS), and biomedicine.

Photoelectrochemical (PEC) etching, with its simplicity and efficiency in the processing of semiconductor materials, holds extensive applications in diverse fields, such as the manufacture of liquid crystal displays and light-emitting diodes (LEDs)[1,2], the fabrication of transformation optics[3], and the surface processing for silicon solar energy and photonic resonators[4,5]. By combining PEC etching with programmable photonic devices such as projectors and spatial light modulators[6], the large-area, fast, and precise patterning of grayscale nanostructures on semiconductor surfaces in a single-shot manner can be achieved, which may further catalyze the applications of PEC etching in microelectronics[7,8], metamaterials[9,10], photovoltaic devices[11,12], and MEMS[13].

Numerous studies have delved into the reaction principles governing the PEC etching process[14–19]. It is generally accepted that a space charge region, similar to a p-n junction, forms at the semiconductor-electrolyte interface, establishing a built-in electric field[6,14,20]. The direction of this electric field is from the interior towards the surface in an n-type semiconductor. When light irradiates the semiconductor surface, electron-hole pairs are generated, after which the holes migrate to the surface under the influence of the electric field, thereby accelerating the surface etching reaction. A prevailing consensus suggests that increasing the irradiance of the incoming light leads to an increased etching rate because more minority carriers will be generated and trek toward the semiconductor surface to catalyze the surface etching process[20].

However, we observed an entirely contrary phenomenon when a structured light field with an intensity gradient is employed to etch an undoped semiconductor wafer, that is, etching is significantly suppressed and accelerated in the high-intensity and low-intensity regions, respectively; see how a Gaussian beam in the PEC etching

[1]State Key Laboratory of Intelligent Manufacturing Equipment and Technology, Huazhong University of Science and Technology, Wuhan, China. [2]Research Institute of Huazhong University of Science and Technology Shenzhen, Shenzhen, China. [3]Optics Valley Laboratory, Wuhan, Hubei, China. [4]State Key Laboratory for Manufacturing Systems Engineering, Xi'an Jiaotong University, Xi'an, Shanxi, China. [5]Department of Biomedical Engineering, The Chinese University of Hong Kong, Hong Kong, China. [6]Department of Mechanical and Energy Engineering, Southern University of Science and Technology, Shenzhen, Guangdong, China. [7]Department of Mechanical Engineering, University of Hong Kong, Hong Kong, China. [8]These authors contributed equally: Pan Peng, Xinqin Liu. ✉e-mail: nicxfang@hku.hk; shyliu@hust.edu.cn; jinlongzhu03@hust.edu.cn

experiments on an undoped semiconductor wafer and an n-type semiconductor wafer leads to the contrary microstructures in Fig. 1a. We theoretically and experimentally demonstrated that the structured light field with an intensity gradient produces a lateral electric field on the surface of the wafer, which is stronger than the built-in electric field of the space-charge region because the undoped wafer has an electrochemical potential close to that of the electrolyte, meaning low band banding conditions by nature. As a result, holes and electrons migrate laterally toward the low-potential area (i.e., the low-intensity area) and the high-potential area (i.e., the high-intensity area), respectively. Because holes catalyze the etching process, while electrons suppress it, the resultant steady-state distribution of holes and electrons leads to accelerated etching in low-intensity areas and suppressed etching in high-intensity areas. We believe this discovery may provide a potential method of large-area and laser-writing technique on undoped semiconductor surfaces, which may find applications in diverse fields such as microelectronics, nanophotonics[21–23], metamaterials, clean energy, and biomedicine.

Results

Experimental system

Figure 1a, c illustrates the schematic and scanning electron microscopy (SEM) (SU3900, Hitachi, Ltd.) images of the etching results, respectively. Figure 1b depicts the in-house developed optical system for demonstrating the anomalous PEC (a-PEC) etching phenomenon alongside its application in the 3D nanofabrication on the surface of an undoped GaAs wafer (see also Supplementary Fig. 4 for the physical diagram of the processing system). In this system, a 532 nm collimated laser (cnilaser-MLL-U-532-SM, Changchun New Industries Optoelectronics Technology Co., Ltd.) beam is spatially filtered by a filter module (consisting of lens L3, the pinhole, and lens L4) after passing through a rotating diffuser to reduce the speckle. The filter module could effectively reduce the instability of the light beam after passing through the rotating diffuser[24]. A phase-only spatial light modulator (SLM) modulates the spatially filtered beam after passing through a linear polarizer and an iris[25]. The Fourier image of the desired light field on the sample plane and the transmissive phase distribution of a Fresnel lens are added to the SLM[26]. The introduced phase of the Fresnel lens can significantly reduce the impact of the zero-order beam[27].

This paper uses the improved Gerchberg-Saxton (GS) algorithm to calculate the desired light field (see Supplementary Note 1)[28]. The distance between the SLM and the iris is designed to be the focal length of the virtual Fresnel lens, such that the reflected light field from the SLM on the iris plane is conjugate to the one on the sample plane. A demagnification system consisting of lens L5 and the objective OBJ is used to achieve the patterning of nanostructures. A complementary metal-oxide-semiconductor (CMOS) transistor camera (GS3-U3-

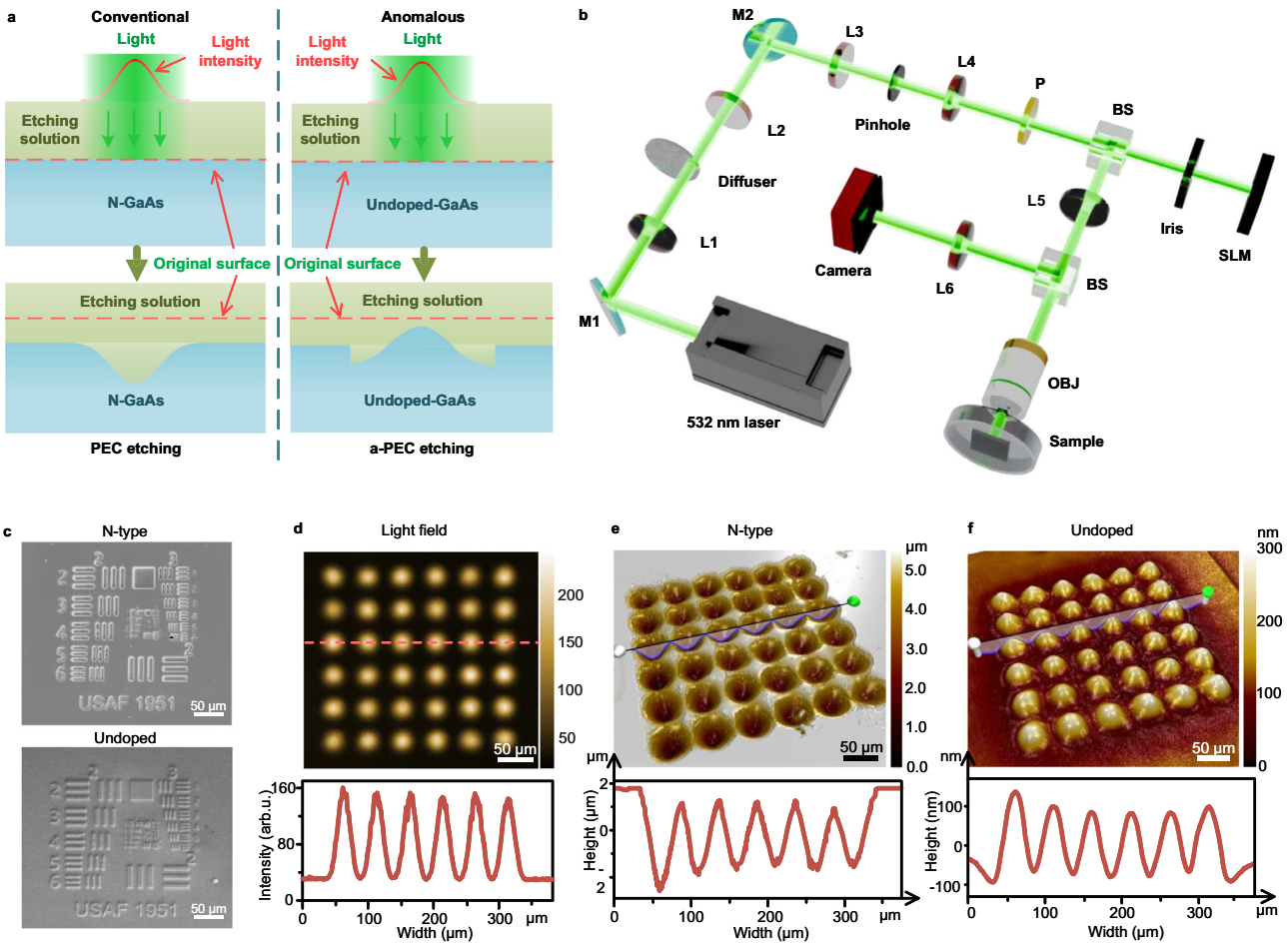

Fig. 1 | Schematic of the anomalous effect in PEC etching and the in-house developed optical fabrication system. a The schematic diagram illustrating the difference between the anomalous phenomenon and the conventional PEC etching. **b** The experimental system consisting of PEC etching and in-situ monitoring modules (L lens, M mirror, P polarizer, BS beam splitter, SLM spatial light modulator, OBJ objective). **c** The SEM images of an etched pattern (i.e., the "USAF 1951" resolution test target pattern) on n-type and undoped GaAs wafers based on a physical photomask. **d** The structured light field of an array of 36 circles captured by the camera. **e** The fabricated microlens array obtained by the conventional PEC etching on an n-doped GaAs wafer. **f** The fabricated microlens array obtained by the a-PEC etching on an undoped GaAs wafer.

https://doi.org/10.1038/s41467-025-63252-1

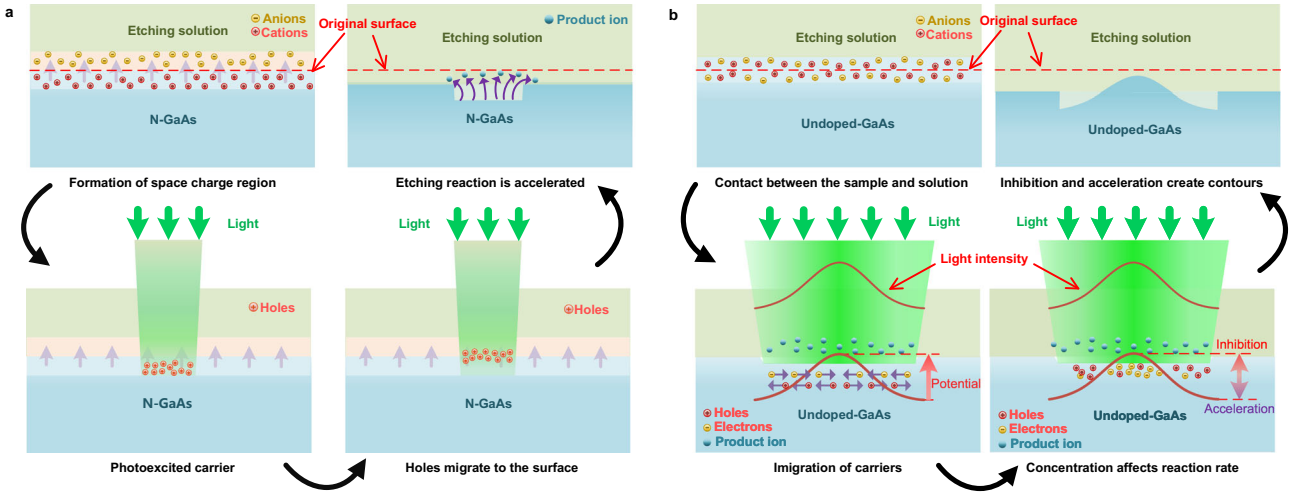

Fig. 2 | The principle of PEC etching and the hypothesis for a-PEC etching. **a** Schematic diagram showing the principle of conventional PEC etching. Photogenerated charge carriers move to the sample surface and catalyze the etching reaction under the built-in electric field. The pink and light blue areas represent the space charge regions of cation accumulation and anion accumulation, respectively. **b** Schematic diagram showing the hypothesis for a-PEC process. The difference in the lateral electric potential generated on the sample surface accelerates the lateral diffusion of charge carriers when illuminated by a structured light field. As a result, the laterally redistributed holes and electrons lead to a completely different etching profile on the surface of undoped semiconductor wafers. The light blue area represents the space charge region.

41C6M-C 1″ FLIR Grasshopper®3) is placed after lens L6, which is conjugated with the sample surface for in-situ monitoring of the surface dynamics of the wafer. Additional details on sample preparation and the specific experimental procedures can be found in the Methods section.

Through this experimental system, we found the etching process on an undoped GaAs wafer resulted in an opposite structure when compared to that on a traditional n-type GaAs wafer (the specific parameters of the wafers are provided in Supplementary Note 5): see how a Gaussian beam could result in a concavity and a convexity on an n-type GaAs wafer and an undoped GaAs wafer respectively in Fig. 1a and an experimentally etching results are provided in Fig. 1c (see Supplementary Fig. 8 for the enlarged figure). We have confirmed that the material of the convexity on the undoped GaAs wafer is Ga and As by spectral analysis (see Supplementary Fig. 9). We further implemented several etching experiments on n-type and undoped GaAs wafers, the first of which is the fabrication of a microlens array (see more details regarding the design of the structured light field in Supplementary Note 1). As shown in Fig. 1d, the generated structured light field, consisting of 6×6 circles with intensity decreasing from the center outward, resulted in opposite etching profiles on the n-type and undoped GaAs wafers; see Fig. 1e, f. This indicates that the undoped GaAs exhibited a low etching rate in the regions with high light intensity, contrary to the etching results in the n-type GaAs wafer. The height difference between the high-light intensity and dark regions in Fig. 1f is almost 100 nm. In comparison, the natural etching depth is 800–1000 nm, considering etching rates in the dark region (80–100 nm min^{-1}) (see Supplementary Fig. 5). This indicates that the structures are lower than the original surface. Thus, we can eliminate the possibility of growth in the high-light intensity regions. Additionally, we conducted experiments to ensure that the electrochemical etching rate is not limited by the area of the cathode reaction (see Supplementary Fig. 13).

Hole concentration dominates the dissolution rate of materials at the semiconductor-electrolyte interface, i.e., the higher the hole concentration, the faster the etching is[29]. Therefore, we can infer that the region illuminated by the weak-intensity light corresponds to a higher hole concentration (see the blue area in Fig. 1f). In comparison, the region illuminated by the high-intensity light corresponds to a lower hole concentration (see the red area in Fig. 1f). Moreover, we observed that the etching is less pronounced in the area far away from the microlens array. However, the intensity of the illuminated light is also weak but non-zero (see the blue area in Fig. 1d and the corresponding yellow outer region in Fig. 1f). This indicates that the intensity of the illuminated light does not directly determine the concentration of holes on the surface of the undoped semiconductor wafer. Furthermore, we observed a noticeable acceleration of etching at the diaphragm's boundary, where the light intensity is weak but the light intensity gradient is quite large. This implies that the light intensity gradient plays a crucial role in determining the distribution of hole concentration (see the deeply etched region around each microlens, where the light intensity gradient is maximal, in Fig. 1f).

Photocarrier transport in a-PEC etching

To investigate how the gradient of light intensity affects the formation of nanostructures on undoped GaAs wafers, we first revisit the etching mechanisms for n-type GaAs and p-type GaAs. A built-in electric field akin to the one in a PN junction forms on the surface when n-type GaAs interfaces with the etchant[30]; see the schematic in Fig. 2a. The built-in vertical electric field drives photogenerated holes towards the interface and thus catalyzes the etching process[31]. In contrast, p-type GaAs presents a distinct scenario where the potential barrier hinders holes from migrating to the interface, making the etching process challenging[32,33]. The conclusion mentioned above drives us to make a hypothesis, that is, the built-in vertical electric field originating from the "PN junction" of the GaAs-etchant interface has a much more substantial impact on the carrier distribution than the lateral electric field induced by the gradient of the illuminated light, when implementing the PEC etching on n-type GaAs wafers. In this case, carriers are predominantly driven vertically toward the surface by the built-in electric field. At the same time, the lateral migration induced by the gradient of light intensity can be neglected. As a result, regions with higher light intensity exhibit higher surface carrier concentration, resulting in a faster etching rate on n-type GaAs wafers.

The concentration of photoinduced holes dominates the dissolution rate of materials at the semiconductor-electrolyte interface; therefore, the higher the hole concentration, the faster the etching is[29]. However, the built-in electric field in the "PN junction" region of an

undoped GaAs wafer is relatively weak when illuminated by the light; see the schematic in Fig. 2b. As a result, the migration of carriers is primarily along the lateral direction because electric field induced by the illuminated structured light field is more substantial than that caused by the "PN junction" of undoped GaAs-etchant interface. This indicates that the number of holes migrating vertically toward the surface will increase if we enhance the impact of the built-in electric field while keeping the structured light field unchanged, resulting in a more pronounced etching effect on the wafer.

We use the same structured light field to illuminate multiple undoped GaAs wafers with different purities to validate this hypothesis. The experimental results confirmed our hypothesis, i.e., that the higher doping density results in a more pronounced etching effect due to the stronger built-in electric field (see Supplementary Figs. 6 and 7). Overall, if the built-in vertical electric field originated from the "PN junction" on the undoped GaAs-etchant interface is significantly weaker than the lateral electric field induced by the gradient of the illuminated light, holes migrate to the region with a low lateral potential caused by the illuminated light. In contrast, the electrons migrate to the region with a high lateral potential.

Surface electrochemical reaction

When the interface between undoped GaAs and the etchant is exposed to nonuniform illumination, the light gradient leads to a horizontal distribution of holes and electrons across the interface. Specifically, the surface concentration ratio of electrons and holes can lead to different surface reaction scenarios[20,34]. When we process with hydrogen peroxide-free etching solution (H_2SO_4: H_2O = 1:25) at a certain light intensity, the illuminated region has no change on the undoped GaAs surface. In contrast, the n-GaAs surface presents a significantly accelerated etching (see Supplementary Fig. 14). This indicates that chemical etching, with the participation of H_2O_2, plays a decisive role in forming surface topography on undoped GaAs. The chemical etching process of GaAs in the mixed solution of H_2SO_4 and H_2O_2 has been proposed in previous research[19,34]. The first step in chemical etching involves a synchronous exchange of bonds between HO—OH and Ga—As surface bonds[35,36]:

$$GaAs + H_2O_2 + Ga^{\cdot} + OH^{\cdot} + As - OH \quad (1)$$

The primary product for both surface atoms is a hydroxide (this may subsequently undergo conversion to oxide), and the Ga—OH bond will be hydrolyzed. When this sequence is twice repeated Ga^{3+} and $As(OH)_3$ are formed as products:

$$GaAs + H_2O_2 + H^+ \rightarrow {Ga^{3+}}_{(aq)} + As(OH)_{3(aq)} \quad (2)$$

The etching rate of this chemical process is determined by the synchronous exchange of bonds in the first step[19]. Three simultaneous exchanges can dissolve one unit of GaAs. When gradient light is irradiated, the etching rate of the process will be affected. Where the concentration of electrons is relatively high, the effect of "photocurrent-doubling" occurs[36]. H_2O_2 first captures a conduction band electron to give an $OH^{\cdot}$ radical:

$$H_2O_2 + e^- \rightarrow OH^- + OH^{\cdot} \quad (3)$$

which subsequently injects a hole into the valence band:

$$OH^{\cdot} \rightarrow OH^- + h^+ \quad (4)$$

Equations (3 and 4) have been proven to suppress chemical etching, the probable reasons being competition for the reactant H_2O_2 or the hydroxide of Ga that adheres to the surface. The effect of hydroxide can be negligible, considering the concentration of H_2SO_4 is 0.04 M[19]. Where the concentration of holes is relatively high, holes could catalyze the oxidative dissolution of GaAs:

$$GaAs + 2H_2O_2 + 2h^+ \rightarrow {Ga(OH)_2}^+ + {AsO_2}^- + 2H^+ \quad (5)$$

The hydroxides of Ga may be hydrolyzed and eventually become Ga^{3+}. The dissolution of GaAs only needs a two-step local electron exchange with H_2O_2, under the catalysis of holes. Hence, the etching rate of reaction 5 is faster than that of 2.

Both light intensity and gradient can affect etching suppression and catalytic dissolution. When the light intensity is constant and the gradient increases, the lateral diffusion of the carriers intensifies, which enhances both reduction (Eqs. (3 and 4)) and oxidation (Eq. 5), resulting in more obvious inhibition and accelerated etching. It is worth noting that when the gradient approaches 0, most carriers undergo surface recombination rather than lateral diffusion. The remaining few carriers can participate in Eqs. (3–5) locally simultaneously, at which point the dissolution rate approaches that of chemical etching. When the gradient is constant and the light intensity increases, the total number of photogenerated carriers increases, resulting in more obvious inhibition and accelerated etching. Equations (3 and 4) are coupled to Eq. (5), which means that the effect of inhibiting etching is similar to that of accelerating etching. In other words, the volume of the convex is close to that of the concave part. This conclusion is valid if the light intensity is high enough to flatten the band bend. When the light intensity is weak (less than 1 mW cm^{-2}), the accelerated etching effect can be more significant (presented in Supplementary Fig. 16) because the band bending on the surface of undoped GaAs makes the surface hole concentration relatively high. The above conclusions were verified in extended experiments in the section: Effects of experimental parameters on surface etching.

Our study highlights a feature of the PEC etching process when an undoped GaAs surface is illuminated with a structured light field; that is, a process called hole-catalyzed oxidation is the key player in areas where the light intensity is lower. This process accelerates the etching by dissolving the material more rapidly than direct chemical etching. On the other hand, in areas where the light is more intense, a different process called the "photocurrent-doubling" effect occurs, which can slow down the dissolution rate. In essence, the intensity of our spatially modulated light can control the speed of the etching process.

Simulation of surface photocarrier behavior

To quantitatively demonstrate that a-PEC etching indeed originated from the gradient of the illuminating light field, we rigorously modeled the built-in vertical electric field and the lateral electric field induced by the "PN junction" and the illuminating light field (see Supplementary Note 6 for the specific simulation process), respectively, using a commercial software SILVACO (Silvaco International Inc.)[37–39]. In Fig. 3a, it is evident that the ratio of electron concentration to hole concentration on the surface of undoped GaAs increases as the light intensity increases, which could result in a more significant inhibition of etching, as per the reaction mechanism mentioned earlier. Our etching results have experimentally validated this under various light intensities (see Supplementary Fig. 3 for more details). As shown in Fig. 3b–e, the vertical potential difference (see Fig. 3e) is much stronger than the lateral potential difference (see Fig. 3c) in the n-type GaAs. In comparison, the vertical potential difference (see Fig. 3d) is weaker than the lateral potential difference (see Fig. 3b) in the undoped GaAs. This demonstrates that the lateral migration of charge carriers is more pronounced than the vertical migration of charge carriers on the surface of undoped GaAs. In contrast, the vertical migration of charge carriers dominates the etching process on the surface of n-type GaAs. We also conducted comparative experiments on p-type GaAs, as presented in Supplementary Note 7, which indicates that in p-type GaAs, where the influence of the built-in electric field is much greater than

https://doi.org/10.1038/s41467-025-63252-1

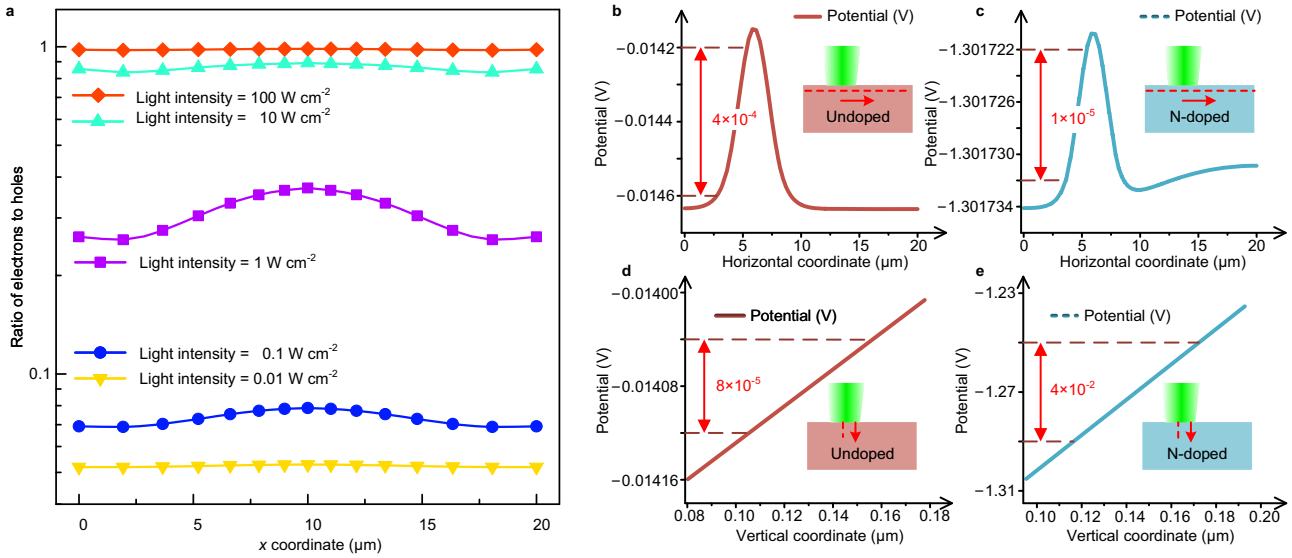

Fig. 3 | Modeling of the gradient of photocarrier concentration and the experimental validation of the principle of a-PEC etching. a Distribution of the ratio of electron concentration to hole concentration on the surface of undoped GaAs under the illumination of Gaussian light fields with different intensities. **b**, **d** Are simulations of the lateral distribution and vertical distribution of the potential near the surface of an undoped GaAs wafer, respectively. **c**, **e** Are simulations of the lateral distribution and vertical distribution of the potential near the surface of an n-type GaAs wafer. The power of the illuminated Gaussian light field is fixed at 2 W cm^{-2}. Source data are provided as a Source data file.

that of the lateral light intensity gradient, the phenomenon of etching acceleration caused by the lateral gradient does not occur.

Effects of experimental parameters on surface etching

Furthermore, we performed extended experiments to determine if or how some factors affect the etching results[40]. The gradient and intensity of light are first studied as the most critical parameters that influence the surface height of the sample after etching. All samples were etched for 10 min. A designed pattern projected on the sample surface is shown in Fig. 4a, in which the light intensities of the central square of the sixteen partitions (each partition consists of a large square and a small cube inside) are almost the same, while the intensities of the peripheral region are increasing from 1 to 16. This design ensures that the gradient in region 1 and region 16 are the largest and smallest, respectively. According to our theory, the cube with the most significant gradient in the upper right corner should produce the highest structure, which has been verified by the etching result shown in Fig. 4b. It can be seen that the height of the cubes is decreasing from region 1 to 16, ignoring the height deviation of the cube at the bottom left which is affected by the gradient at the edge of the pattern. The experimental results agree well with our theoretical analysis. We then presented the surface height h of the etched cubes as a function of the gradient g in Fig. 4c (defined as $g = (I_1 - I_2)/I_1$, in which I_1 and I_2 are the optical power density at the central cube and peripheral region, respectively). As shown in Fig. 4c, the height h of the cube indeed increases as the light-intensity gradient increases. We then use another pattern of four circles shown in Fig. 4d to verify the relationship between height and light intensity. The corresponding gradient of the circles is almost the same when light intensity varies within a small range (a significant difference in light intensity will result in a large difference in image contrast, leading to a substantial change in the gradient). Here, we presented the relation of surface height h (the average height of the circle relative to the unilluminated region) after etching as a function of light intensities ranging from 6 to 18 mW cm^{-2} in Fig. 4f, while the gradient is near 0.466, 0.522, 0.728, and 0.851, respectively. The data indicate that the height increases with the increase in light intensity at a fixed gradient condition. In summary, light intensity and gradient simultaneously affect height. Light intensity represents the optical power density of a point, and gradient represents the difference in optical power density between a point and its surrounding points. Thus, the height at a specific point on the etched sample surface is affected by the optical power density at that point and in the surrounding areas. The lateral diffusion of carriers determines the surrounding range.

The lateral diffusion of carriers plays an important role in forming surface topography during the etching process[41,42]. We designed four patterns shown in Fig. 4g, each featuring a square area with uniformly distributed light intensity. The dimensions of the squares differ among the patterns, while the total illumination area is the same. The etching results are presented in Fig. 4h. The etched profile across different pattern sizes presents significant variations. Specifically, the smaller rectangles are etching suppressed, and there was minimal height difference between each rectangle's edge and central area. However, in the case of larger rectangles, suppression of etching was observed only at the edges, while the central area was etching-accelerated. According to our theory, the lateral migration of carriers affected by the light gradient causes apparent etching and inhibition of etching at the edge, after which the carriers spread laterally between the edge region and the center region until equilibrium is reached. Based on the above analysis, we can conclude that a flat surface is obtained after etching for patterns of uniform light intensity with small dimensions (here, it is less than ≈50 μm). For uniform patterns with large dimensions (here, >200 μm), the middle area is a plane, while a curved outline appears at the edge after etching. The situation between these two sizes will produce a concave. From these results, we can see that the rate of structure formation is related to the structure's light intensity, gradient, and size, all of which are fixed for a given etching solution. Per our experiments, the maximum rate does not exceed the chemical etching rate (100 nm min^{-1}). Additionally, we verified that the etching topography does not exhibit significant changes over time, as the light field remains consistent when the etching depth is small. Furthermore, our findings indicate that polarization does not influence the etching topography. Detailed information regarding these experiments is provided in the Supplementary Note 3.

The experiments above demonstrate that we can achieve precise 3D nanofabrication on undoped semiconductor wafers by controlling

https://doi.org/10.1038/s41467-025-63252-1

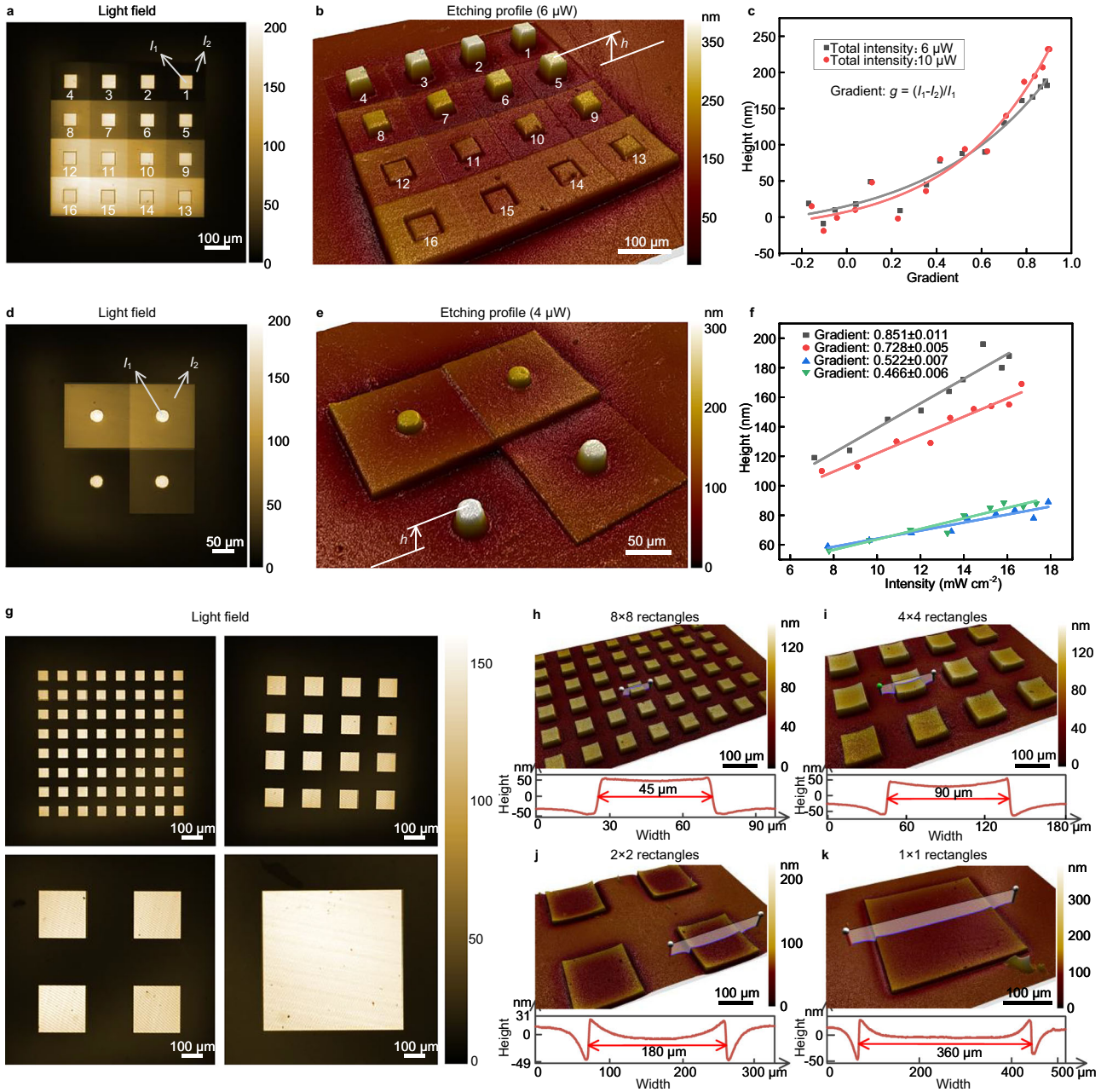

Fig. 4 | Experimental validation for the effects of intensity and gradient. a The structured light field consisting of sixteen square areas numbered from 1 to 16, each with the same light intensity of the small square in the center and a different light intensity of the peripheral region. **b** The etching results of a-PEC etching using the light field **a** with a total intensity of 6 μW, where *h* means the average height of the central square relative to the unilluminated region. **c** The relationship between height *h* and gradient *g* (defined as $g = (I_1 - I_2)/I_1$, in which I_1 and I_2 are the optical power density of the central square and peripheral region, respectively). **d** The structured light field consisting of four partitions, each with the same light intensity as the central small circular area and a different light intensity in the peripheral region. **e** The etching results using the light field **d** with a total intensity of 4 μW. **f** The relationship between height *h* and light intensity *I* (the optical power intensity of the central circular area). **g** The structured light field consisting of four rectangular arrays of different sizes. **h**, **i**, **j**, **k** Are the etching results of 8 × 8, 4 × 4, 2 × 2, and 1 × 1 rectangles, respectively, by using the light field **g**. Source data are provided as a Source data file.

both the gradient and intensity of the incoming light (see Fig. 4 for an explanation of how the gradient and intensity of light could control the 3D nanofabrication process).

Surface nanofabrication

The revealed mechanism of a-PEC etching indicates that we can create grayscale nanostructures and planar 2D nanostructures on the surface of undoped semiconductor materials by customizing the gradient distribution and intensity of the incoming light field. The critical dimension achievable by our method is diffraction-limited; see Supplementary Note 4 for more details regarding the resolution tests. Additionally, we have presented the surface height of the etched structures as a function of the gradient, light intensity, and the etching time, as shown in Supplementary Fig. 19, demonstrating the precise height control of this method. The structures shown in Fig. 5a–c, including a spiral line structure with its height diminishing from the inside out, a logo "HUST," and a concentric ring structure, highlight the adaptability of this approach, as altering the light field pattern allows for flexible modification of the structures' characteristics (another pattern named "USAF 1951" resolution test target can be found in

https://doi.org/10.1038/s41467-025-63252-1

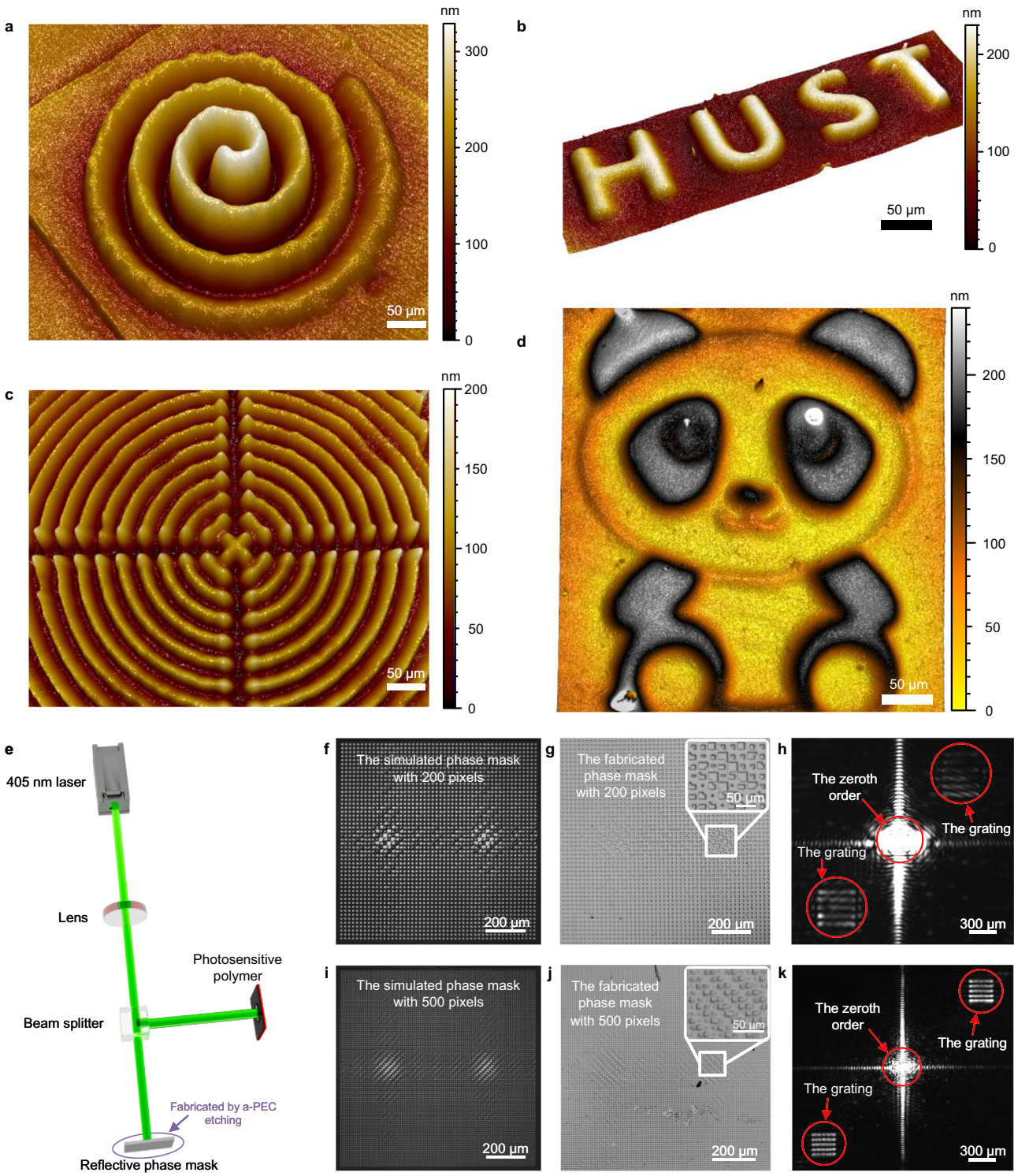

Fig. 5 | Grayscale nanostructures fabricated using a-PEC etching on undoped GaAs wafers. a The spiral with decreasing light intensity from the center outward. **b** The logo "HUST" (Huazhong University of Science and Technology). **c** The concentric ring structure separated by two vertical lines. **d** The grayscale panda-like structure. **e** The in-house developed holographic lithography system. **f** The simulated 200 pixels phase mask for holographic imaging. **g** The fabricated 200 pixels phase mask for holographic imaging. **h** The holographic imaging results of the 200 pixels phase mask. **i** The simulated 500 pixels phase mask for holographic imaging. **j** The fabricated 500 pixels phase mask for holographic imaging. **k** The holographic imaging results of the 500 pixels phase mask.

Supplementary Fig. 8). Furthermore, this method is well-suited for the fabrication of grayscale nanostructures, owing to its capacity to control the height of nanostructures, exemplified by the grayscale panda-like structure showcased in Fig. 5d. The a-PEC etching can also be employed as a cost-effective and highly efficient method to fabricate the reflective phase mask for holographic lithography. Holographic lithography, which utilizes light interference to generate a light pattern into the photosensitive polymer (see the schematic of an in-house developed holographic lithography system in Fig. 5e and Supplementary Fig. 10)[43–49], has been demonstrated as a viable platform for rapid and scalable manufacturing of nanostructures[50,51]. A photomask can be fabricated using conventional methods such as e-beam

lithography and direct laser writing, but they are typically slow and costly due to the raster scanning mode[52–55]. In contrast, the proposed etching method enables the direct fabrication of grayscale or 2D patterns on a semiconductor surface in a single-shot manner. The patterned semiconductor surface can be used as the reflective phase mask in a holographic lithography system; see the simulated and fabricated reflective phase masks in Fig. 5f, g. The holographic images (i.e., the gratings and the zeroth diffraction orders) resulting from the phase masks with large and small pixel sizes are shown on the right side of Fig. 5f, g. The smaller the pixel size in the phase mask, the higher the resolution of the holographic images. Moreover, we can observe that defects introduced in the phase mask during the etching process do not significantly impact the results of holographic imaging, because the phase mask we processed modulates the light field in the frequency domain. This indicates a high fault tolerance in this application. The capability of directly fabricating 2D and grayscale nanostructures on semiconductor surfaces in a single-shot manner without the use of photoresist demonstrates that our prototype fuses the capabilities of a stepper as well as an etcher, which may find applications in nanophotonics, biomedicine, and microelectronics.

Discussion

Our study revealed an anomalous phenomenon: the structures fabricated on undoped semiconductor surfaces are opposite to those on n-type semiconductor surfaces after PEC etching. We theoretically and experimentally demonstrated that this phenomenon is attributed to the lateral redistribution of carriers prompted by the gradient of the illuminated light field. Our experimental studies revealed that a-PEC etching can be achieved with a minimal critical dimension close to the optical diffraction limit at the maximal rate (100 nm min^{-1}). Moreover, we found that a-PEC etching is very sensitive to the gradient. For example, our experiments have demonstrated that a-PEC etching occurs only if the gradient exists, and the required gradient value is closely related to the optical power density. This phenomenon and mechanism can provide some enlightenment for the surface photoelectrochemical process of semiconductors. Additionally, the a-PEC etching has the potential for fabricating a phase mask due to its nm-level accuracy in height control and near-diffraction limit resolution. This discovery provides a rapid and large-scale 3D nanomanufacturing technique for undoped semiconductor materials by simply customizing the gradient and intensity of an illumination light field, which may find applications in diverse fields such as microelectronics, nanophotonics, MEMS, clean energy, and biomedicine.

Methods

Materials

Sulfuric acid (H_2SO_4, 10%), hydrogen peroxide (H_2O_2, 30%), and ultrapure water purchased from Shengshi Standard (Xiamen) Technology Co., Ltd were mixed according to the volume ratio to prepare the etching solution. Isopropyl alcohol (IPA, 99.5%) was purchased from Shandong Xiya Chemical Co., Ltd. Deionized (DI) water was supplied by Suzhou Industrial Distilled Water Co., Ltd. The n-type GaAs (100) with a doping concentration of $Nd = 3 \times 10^{18}\,cm^{-3}$ and undoped GaAs (100) with a resistivity of $4 \times 10^8\,\Omega$ cm were supplied by Innotronix Technologies Co., Ltd. The p-type GaAs (100) with a doping concentration of $Nd = 1.9 \times 10^{19}\,cm^{-3}$ was supplied by Suzhou Leilichang Semiconductor Co., LTD.

Sample preparation

The following steps remove contaminants from the sample surface. Firstly, we remove organic residues on the sample surface by immersing the sample in a solution of isopropyl alcohol and subjecting it to ultrasonic cleaning for 10 min. Subsequently, sulfuric acid removes inorganic contaminants. After each of the steps above, a thorough rinse of the sample is necessary to ensure the residual cleaning agents and contaminants are removed. Finally, we clean all the remaining impurities by subjecting the sample to ultrasonic waves in deionized water. When the cleaning process is completed, the sample is dried using a nitrogen gun to prevent the introduction of contaminants, after which the dried sample is stored in a clean environment for future experiments.

Optical power density calculation

In all experiments, a digital optical power and energy meter (PM100, Thorlabs Co., Ltd.) was used to measure the optical power (P) of the pattern projected directly after the objective lens, approximating the optical power incident on the sample surface. The optical power density I was calculated by $I = P/A$, where A is the total area of the processed pattern.

Processing operation

The n-type GaAs (100) with a doping concentration of $Nd = 3 \times 10^{18}\,cm^{-3}$ and undoped GaAs (100) with a resistivity of $4 \times 10^8\,\Omega$ cm are cut into 0.8 × 0.8 cm pieces and placed in a glass Petri dish without electrical contact, which is mounted on a motorized x-y-z stage to ensure accurate positioning and in-focal fabrication. Each experiment is performed on a different piece. A standard etchant (H_2SO_4: H_2O_2: H_2O = 1: 1: 25) was poured into the container with a depth of 5 mm, which was changed after each etching process to ensure the accuracy of the comparison experiment. Then, the phase diagram is loaded onto the SLM, followed by the focus adjustment. When focusing is completed, we turn off the light source and then move the sample 2 mm along the x-axis to ensure the following a-PEC etching is implemented in an unexposed region. We then turn the light source back on for a-PEC etching. All of the samples were etched for 10 min. We monitor the etching dynamics using a regular camera (GS3-U3-41C6M-C 1″ FLIR Grasshopper®3).

3D surface measurement and analysis for the fabricated nanostructures

The 3D profiles of the etched samples were measured using a commercial white light interferometer (ER230-Atometrics) with a 20× objective. We used a commercial white light interferometer with a 20× objective to measure the profile of the fabricated 3D nanostructure on undoped GaAs wafers. The resulting vertical and lateral resolution can reach 1 nm and 400 nm, respectively. MountainsMap® generates all three-dimensional images and cross-sectional profiles.

Photocarrier simulation

We utilize the device simulator, Atlas, part of the software suite Silvaco, to simulate the distribution of carrier concentration and electric field on the GaAs surface under illumination.

Data availability

The data that support the findings of this study are available from the corresponding authors upon request. Source data are provided with this paper.

References

1. Kneissl, M., Seong, T.-Y., Han, J. & Amano, H. The emergence and prospects of deep-ultraviolet light-emitting diode technologies. *Nat. Photonics* **13**, 233–244 (2019).
2. Doan, V. V. & Sailor, M. J. Luminescent color image generation on porous silicon. *Science* **256**, 1791–1792 (1992).
3. Barth, D. S. et al. Macroscale transformation optics enabled by photoelectrochemical etching. *Adv. Mater.* **27**, 6131–6136 (2015).
4. Gil-Santos, E. et al. Scalable high-precision tuning of photonic resonators by resonant cavity-enhanced photoelectrochemical etching. *Nat. Commun.* **8**, 14267 (2017).

5. Ren, S. et al. Interface-confined surface engineering via photoelectrochemical etching toward solar neutral water splitting. *ACS Catal.* **12**, 1686–1696 (2022).
6. Kohl, P. A. & Harris, D. B. Photoelectrochemical methods for semiconductor device processing. *Electrochim. Acta* **38**, 101–106 (1993).
7. Yates, J. T. A new opportunity in silicon-based microelectronics. *Science* **279**, 335–336 (1998).
8. Noyce, R. N. Microelectronics. *Sci. Am.* **237**, 62–69 (1977).
9. Zheludev, N. I. & Kivshar, Y. S. From metamaterials to metadevices. *Nat. Mater.* **11**, 917–924 (2012).
10. Fusco, Z. et al. Photonic fractal metamaterials: a metal–semiconductor platform with enhanced volatile-compound sensing performance. *Adv. Mater.* **32**, 2002471 (2020).
11. Wang, L. et al. 2D photovoltaic devices: progress and prospects. *Small Methods* **2**, 1700294 (2018).
12. Sariciftci, N. S. Plastic photovoltaic devices. *Mater. Today* **7**, 36–40 (2004).
13. Spearing, S. M. Materials issues in microelectromechanical systems (MEMS). *Acta Mater.* **48**, 179–196 (2000).
14. Haroutiounian, E., Sandino, J. P., Cléchet, P., Lamouche, D. & Martin, J. R. Electrochemical and photoelectrochemical behavior and selective etching of III–V semiconductors in H 2 O 2 as redox system. *J. Electrochem. Soc.* **131**, 27 (1984).
15. Park, S.-M. & Barber, M. E. Thermodynamic stabilities of semiconductor electrodes. *J. Electroanal. Chem. Interfacial Electrochem.* **99**, 67–75 (1979).
16. Carrabba, M. M., Nguyen, N. M. & Rauh, R. D. Effects of doping and orientation on photoelectrochemically etched features in n - GaAs. *J. Electrochem. Soc.* **134**, 1855 (1987).
17. Lowes, T. D. & Cassidy, D. T. Photochemical etching of n-InP as a function of temperature and illumination. *J. Appl. Phys.* **68**, 814–819 (1990).
18. Ruberto, M. N. et al. The laser-controlled micrometer-scale photoelectrochemical etching of III–V semiconductors. *J. Electrochem. Soc.* **138**, 1174 (1991).
19. van Dorp, D. H. et al. Nanoscale etching of III-V semiconductors in acidic hydrogen peroxide solution: GaAs and InP, a striking contrast in surface chemistry. *Appl. Surf. Sci.* **465**, 596–606 (2019).
20. Kohl, P. A. Photoelectrochemical etching of semiconductors. *IBM J. Res. Dev.* **42**, 629–638 (1998).
21. Podlesnik, D. V., Gilgen, H. H., Osgood, R. M. Jr. & Sanchez, A. Maskless chemical etching of submicrometer gratings in single-crystalline GaAs. *Appl. Phys. Lett.* **43**, 1083–1085 (1983).
22. Ostermayer, F. W. Jr., Kohl, P. A. & Burton, R. H. Photoelectrochemical etching of integral lenses on InGaAsP/InP light-emitting diodes. *Appl. Phys. Lett.* **43**, 642–644 (1983).
23. Liu, X. et al. Rewritable ITO patterning for nanophotonics. *Laser Photonics Rev.* **19**, 2401799 (2025).
24. Kumar, V. et al. Speckle noise reduction strategies in laser-based projection imaging, fluorescence microscopy, and digital holography with uniform illumination, improved image sharpness, and resolution. *Opt. Laser Technol.* **141**, 107079 (2021).
25. Peng, Y., Choi, S., Kim, J. & Wetzstein, G. Speckle-free holography with partially coherent light sources and camera-in-the-loop calibration. *Sci. Adv.* **7**, eabg5040 (2021).
26. Lee, M., Koo, D. & Kim, J. Simple and fast calibration method for phase-only spatial light modulators. *Optics Lett.* **48**, 5–8 (2022).
27. Zwick, S., Haist, T., Warber, M. & Osten, W. Dynamic holography using pixelated light modulators. *Appl. Opt.* **49**, F47–F58 (2010).
28. Zhang, C. et al. Optimized holographic femtosecond laser patterning method towards rapid integration of high-quality functional devices in microchannels. *Sci. Rep.* **6**, 33281 (2016).
29. Ostermayer, F. W. Jr., Kohl, P. A. & Lum, R. M. Hole transport equation analysis of photoelectrochemical etching resolution. *J. Appl. Phys.* **58**, 4390–4396 (1985).
30. Rajeshwar, K. Electron Transfer at Semiconductor-Electrolyte Interfaces. *In: Electron Transfer in Chemistry* (2001).
31. Khare, R. & Hu, E. L. Dopant selective photoelectrochemical etching of GaAs homostructures. *J. Electrochem. Soc.* **138**, 1516 (1991).
32. Ostermayer, F. W. Jr. & Kohl, P. A. Photoelectrochemical etching of p-GaAs. *Appl. Phys. Lett.* **39**, 76–78 (1981).
33. Andersen, O. K., Frello, T. & Veje, E. Photoinduced synthesis of porous silicon without anodization. *J. Appl. Phys.* **78**, 6189–6192 (1995).
34. Gerischer, H. & Mindt, W. The mechanisms of the decomposition of semiconductors by electrochemical oxidation and reduction. *Electrochim. Acta* **13**, 1329–1341 (1968).
35. Minks, B. P., Vanmaekelbergh, D. & Kelly, J. J. Current-doubling, chemical etching and the mechanism of two-electron reduction reactions at GaAs: Part 2. A unified model. *J. Electroanal. Chem. Interfacial Electrochem.* **273**, 133–145 (1989).
36. Minks, B. P., Oskam, G., Vanmaekelbergh, D. & Kelly, J. J. Current-doubling, chemical etching and the mechanism of two-electron reduction reactions at GaAs: Part 1. Experimental results for H2O2 and Br2. *J. Electroanal. Chem. Interfacial Electrochem.* **273**, 119–131 (1989).
37. Belarbi, M., Beghdad, M. & Mekemeche, A. Simulation and optimization of n-type interdigitated back contact silicon heterojunction (IBC-SiHJ) solar cell structure using Silvaco TCAD Atlas. *Sol. Energy* **127**, 206–215 (2016).
38. Michael, S. & Bates, A. The design and optimization of advanced multijunction solar cells using the Silvaco ATLAS software package. *Sol. Energy Mater. Sol. Cells* **87**, 785–794 (2005).
39. Michael, S., Bates, A. D. & Green, M. S. Silvaco ATLAS as a solar cell modeling tool. In: *Conference Record of the Thirty-first IEEE Photovoltaic Specialists Conference, 2005*.) (2005).
40. Ryan, M. A., Levy-Clement, C., Mahalu, D. & Tenne, R. A New process for optical data recording by photoelectrochemical etching. *Ber. Bunsenges. für Physikalische Chem.* **94**, 671–676 (1990).
41. Nobuaki Noguchi, N. N. & Ikuo Suemune, I. S. High-resolution patterning of luminescent porous silicon with photoirradiation. *Jpn. J. Appl. Phys.* **33**, 590 (1994).
42. Noguchi, N. & Suemune, I. Selective formation of luminescent porous silicon by photosynthesis. *J. Appl. Phys.* **75**, 4765–4767 (1994).
43. Gabor, D. A new microscopic principle. *Nature* **161**, 777–778 (1948).
44. Lee, J. et al. Proximity-field nanopatterning for high-performance chemical and mechanical sensor applications based on 3D nanostructures. *Appl. Phys. Rev.* **9**, 011322 (2022).
45. Nam, S.-H. et al. Fundamental principles and development of proximity-field nanopatterning toward advanced 3D nanofabrication. *Nano Res.* **14**, 2965–2980 (2021).
46. Park, J. et al. Three-dimensional nanonetworks for giant stretchability in dielectrics and conductors. *Nat. Commun.* **3**, 916 (2012).
47. Kondo, T., Juodkazis, S., Mizeikis, V., Misawa, H. & Matsuo, S. Holographic lithography of periodic two-and three-dimensional microstructures in photoresist SU-8. *Opt. Express* **14**, 7943–7953 (2006).
48. Dalisa, A. L., Zwicker, W. K., DeBitetto, D. J. & Harnack, P. Photoanodic engraving of holograms on silicon. *Appl. Phys. Lett.* **17**, 208–210 (1970).
49. Wei, D. T. Y. & Bloom, L. R. Photoanodic engraving as a means of making a relief hologram on photoconductor surfaces. *Appl. Opt.* **12**, 150–152 (1973).

50. Kagias, M. et al. Metasurface-enabled holographic lithography for impact-absorbing nanoarchitected sheets. *Adv. Mater.* **35**, 2209153 (2023).
51. Campbell, M., Sharp, D. N., Harrison, M. T., Denning, R. G. & Turberfield, A. J. Fabrication of photonic crystals for the visible spectrum by holographic lithography. *Nature* **404**, 53–56 (2000).
52. Groves, T. R. 3 - Electron beam lithography. In: *Nanolithography* (ed Feldman M). (Woodhead Publishing, 2014).
53. Weichelt, T., Bourgin, Y., Banasch, M. & Zeitner, U. D. Advanced photomask fabrication by e-beam lithography for mask aligner applications. In: *Proc.* 32nd European Mask and Lithography Conference (SPIE, 2016).
54. Venkatakrishnan, K. et al. Laser writing techniques for photomask fabrication using a femtosecond laser. *Appl. Phys. A* **74**, 493–496 (2002).
55. Guo, C. F. et al. Grayscale photomask fabricated by laser direct writing in metallic nano-films. *Opt. Express* **17**, 19981–19987 (2009).

Acknowledgements

This work was funded by National Nature Science Foundation of China (Grant No. 52175509) to J.Z., National Key Research and Development Program of China (2023YFF1500900) to N.F., Shenzhen Fundamental Research Program (JCYJ20220818100412027) to H.D., China National Funds for Distinguished Young Scientists (No. 52225507) to S.Y., Guangdong-Hong Kong Technology Cooperation Funding Scheme Category C Platform (SGDX20230116093543005) to J.Z., and Innovation Project of Optics Valley Laboratory (Grant No. OVL2023PY003) to S.L. Thanks to engineers Pan Li in Optoelectronic Micro&Nano Fabrication and Characterizing Facility, Wuhan National Laboratory for Optoelectronics of Huazhong University of Science and Technology, for the support in device fabrication. We thank Dr. Ye Ma from the Core Facility of Wuhan University for assistance with AFM analysis.

Author contributions

J.Z. conceived the idea. P.P. developed the theoretical analysis and TCAD simulations. P.P. and X.L. performed the experiments. J.Z., S.Y., R.Z., H.D., L.G., N.F., and S.L. supervised and coordinated all the work. All authors commented on the manuscript. P.P. and X.L. contributed equally to this work.

Competing interests

The authors declare no competing interests.

Additional information

Supplementary information The online version contains supplementary material available at https://doi.org/10.1038/s41467-025-63252-1.

Correspondence and requests for materials should be addressed to Nicholas X. Fang, Shiyuan Liu or Jinlong Zhu.

Peer review information *Nature Communications* thanks the anonymous reviewers for their contribution to the peer review of this work. A peer review file is available.